Petroleum Science 23 (2026) 5096–5110

Contents lists available at ScienceDirect

Petroleum Science

journal homepage: www.keaipublishing.com/en/journals/petroleum-science

Original Paper

Investigation of the effect of water-vapour-containing hydrogen-blended natural gas fraction on the condensation performance of a Laval nozzle using BBD and PSO

Guan-Wei Jia [a,*], Kai-Feng Xue [a], Rui Li [b]

[a] School of Physics and Electronics, Henan University, Kaifeng, 475004, Henan, China
[b] PipeChina Institute of Science and Technology, Tianjin, 300457, China

A R T I C L E I N F O

Article history:
Received 22 November 2025
Received in revised form
3 February 2026
Accepted 6 May 2026
Available online 12 May 2026

Edited by Xi Zhang

Keywords:
Hydrogen-blended natural gas
Laval nozzle
Box–Behnken design
Particle swarm algorithm
Water vapour condensation

A B S T R A C T

Hydrogen-blended natural gas delivered via pipeline networks supports the development of hydrogen energy. However, hydrogen-blended natural gas containing water vapour significantly decreases delivery efficiency and accelerates pipeline corrosion, necessitating rigorous dewatering before transportation, storage, and utilisation. This mixture is primarily methane-based, with component variations depending on the source. This study employs Box–Behnken design (BBD) and particle swarm optimisation (PSO) to examine how the composition and content of hydrogen-blended natural gas influence the condensation rate in Laval nozzles. Utilising computational fluid dynamics (CFD), we calculated the flow parameters of various hydrogen-blended natural gas fractions and contents through the Laval nozzle. The optimal gas composition was identified using BBD and PSO, resulting in a condensation rate of 78.65% with CH_4 at 69.212%, C_2H_6 at 2.028%, C_3H_8 at 1.107%, and H_2 at 9.01%. This condensation rate is significantly higher compared to mixtures containing only CH_4 and H_2. These findings guide the investigation of phase transformation mechanisms in multi-component condensation of hydrogen-blended natural gas with water vapour and their engineering applications.

1. Introduction

The climate crisis has become a central driver for accelerating the energy transition; although natural gas is a cleaner fossil fuel, its direct combustion still emits carbon (Jiang et al., 2024). Hydrogen energy is a pivotal focus in the global energy transition due to its zero carbon emissions, high energy density, renewability, and adaptability across multiple scenarios (Blay-Roger et al., 2024). Hydrogen is regarded as the 'ultimate energy source'. However, directly replacing natural gas must overcome significant barriers in production, storage, transportation, utilisation, and cost (Acar and Dincer, 2019). To address these challenges, numerous governments have integrated hydrogen energy into their strategic plans. China's hydrogen policy is driven by a national strategy aimed at promoting the hydrogen industry as a new engine for energy transformation and high-quality economic development (Zhang et al., 2022). In contrast, the U.S. hydrogen policy centres on decarbonization, establishing regional hydrogen energy hubs and facilitating the large-scale expansion of the hydrogen sector (Madadi Avargani et al., 2022). Meanwhile, the European hydrogen strategy focuses on achieving carbon neutrality and energy security by constructing an industry-wide framework through the EU Hydrogen Energy Strategy (Gatto et al., 2024). Currently, hydrogen production costs are high, with green hydrogen priced between $2.5–3.5/kg, necessitating a reduction to $0.8–1/kg to compete with natural gas (Choi et al., 2024). Additionally, hydrogen's low density, susceptibility to leakage, and high storage and transportation costs in conventional high-pressure gaseous or liquid forms present further obstacles (Zhang et al., 2024). Hydrogen-blended natural gas technology serves as a pivotal transitional initiative in the energy shift, enabling the gradual development of the hydrogen industry chain and laying the foundation for future pure hydrogen supply (Abdin, 2024). This blending can significantly reduce carbon intensity and

* Corresponding author.
E-mail address: jiaguanwei@henu.edu.cn (G.-W. Jia).
Peer review under the responsibility of China University of Petroleum (Beijing).

https://doi.org/10.1016/j.petsci.2026.05.002
1995-8226/

accelerate progress toward net-zero emission targets (Neacsa et al., 2023). Moreover, transporting hydrogen through existing natural gas pipeline networks can avoid the substantial investments required to build new pure hydrogen pipelines and lower the terminal usage costs of hydrogen energy (Ogden et al., 2018). In the application of hydrogen-blended natural gas, research on its terminal combustion utilisation has also garnered significant attention. Changes in its combustion characteristics, flame stability, and pollutant emissions represent current research hotspots. Hydrogen-blended natural gas technology constitutes a systematic engineering project encompassing the entire "production-transportation-application" chain. Conducting in-depth research on its dehydration and purification behaviour during transportation is an indispensable component for ensuring the safe and efficient operation of the entire chain (Shan et al., 2025).

Water vapour is unavoidable during the production and storage of natural gas and hydrogen. A significant amount of water vapour is generated during natural gas extraction (Sun et al., 2022) and hydrogen production through chemical reactions (El-Emam and Özcan, 2019). High-pressure natural gas extracted from gas wells typically contains free water and pressurized water vapour. Water vapour is also generated during processes such as hydrogen production via water electrolysis, industrial byproduct hydrogen preparation, thermochemical water splitting, and photolysis of water (Cavana et al., 2021). During natural gas transportation, external moisture readily infiltrates pipelines if sealing issues exist. These represent primary sources of water vapour in high-pressure natural gas and hydrogen production. Temperature and pressure fluctuations within pipelines during transport may cause water vapour to condense and form liquid accumulation. Within natural gas pipelines, water vapour reduces transmission efficiency, leads to hydrate formation that exacerbates pipeline corrosion, and notably affects pipeline safety and economic operations (Farhadian et al., 2023). Therefore, thorough dewatering and purification of hydrogen-blended natural gas are essential prior to its transportation, storage, and use. To remove water vapour from hydrogen-blended natural gas, existing natural gas dehydration technologies are primarily applicable (Netusil and Ditl, 2011). Water vapour is absorbed using polar hygroscopic agents or porous adsorbents; however, this process remains energy intensive (Júnior and Filho, 2023). Physical adsorption via porous media is utilised for water vapour dehydration but is limited by temperature and pressure conditions (Rouzbahani et al., 2014). The selective permeability of membrane materials allows for water vapour separation through preferential permeability mechanisms; nonetheless, long-term operation is vulnerable to membrane surface contamination and pore clogging (He et al., 2020). Using a Laval nozzle for ultrasonic separation of water vapour from natural gas presents benefits such as a simple device structure, lack of moving parts, and no need for chemicals (Wen et al., 2020). Consequently, the processes of production, blending, dewatering, transportation, and application of hydrogen-blended natural gas containing water vapour are illustrated in Fig. 1.

Hydrogen-blended natural gas consists of hydrocarbon gases, non-hydrocarbon gases, and hydrogen (Faramawy et al., 2016). As Table 1 shows, the molecular weight of H_2 is 2 g/mol, significantly lower than that of CH_4 at 16 g/mol. Hydrogen blending reduces the density of the mixture, affecting its Mach number variation and expansion characteristics within the nozzle. H_2 possesses a different isothermal specific heat capacity compared to CH_4, which influences changes in temperature, pressure distribution, and subcooling during gas expansion within the nozzle. After hydrogen is blended into natural gas, condensation models for pure natural gas or existing binary/ternary natural gas mixtures can no longer be applied simplistically. Condensation in multi-component hydrogen-blended natural gas involves complex coupled processes of heat transfer, mass transfer, and phase-change kinetics.

The gas components and their contents in natural gas vary in different regions (Economides and Wood, 2009). The micromechanisms of supercooling nucleation and droplet growth are fundamental to the study of supersonic condensation and provide the theoretical foundation for condensing water vapour in Laval nozzles (Yang and Shen, 2009). To improve the efficiency of condensing water vapour in hydrogen-blended natural gas containing water, it is essential to investigate the condensation process (Chen et al., 2023). Numerous studies have explored the characteristics of natural gas condensation in supersonic flows. Castier (2014) examined the spontaneous condensation of water vapour within a convergent dispersive nozzle using phase equilibrium theory. Zhang et al. (2017) found that latent heat is released during the condensation of water vapour in Moses and Stein nozzles and that condensation occurs only when vapour subcooling reaches a critical threshold. Jiang et al. (2016) investigated the supersonic condensation of CH_4–H_2O–C_9H_{20} mixtures. They observed that spontaneous condensation of water vapour began 4 mm behind the throat of the Laval nozzle, with water vapour droplets acting as nuclei for the condensation of C_9H_{20}, which condenses at a supercooling of 38.3 K.

Cao and Yang (2015) analysed the differences in the passage of N_2–H_2O and CH_4–H_2O through the nozzle. The results showed that for different binary compounds containing the same condensable gas system, the condensation parameter trends are consistent, with the specific heat of the carrier gas being the dominant factor. Sun et al. (2024) utilised supersonic separation in conjunction with the Euler–Euler model to investigate the condensation characteristics of H_2O, CO_2, H_2S, and nC_9H_{20} in CH_4. The findings indicate that H_2O and nC_9H_{20} are highly sensitive to calibration factors. Yan et al. (2025) analysed and compared the condensation processes of various hydrogen-blended natural gas fractions from Iran, the USA, Russia, and Australia within a Laval nozzle. Their results demonstrate that the Russian hydrogen-blended natural gas fraction exhibits the highest condensation rate, reaching 79.63% within the nozzle. Bian et al. (2019) examined the supersonic condensation process of CH_4–C_2H_6 binary mixtures, elucidating the mechanisms of nucleation and droplet growth. They found that C_2H_6 vapour attains the critical radius first, leading to its initial condensation and nucleation. The composition and concentrations of water-containing hydrogen-blended natural gas significantly influence the distribution of the condensate vapour flow field and the condensation effects within the Laval nozzle.

The Box–Behnken design (BBD) offers an efficient and safe approach for multifactor test optimisation by reducing the number of trials (Ferreira et al., 2007). The particle swarm optimisation (PSO) demonstrates robust global search capabilities and parallelism in multiparameter analysis through its unique group intelligence mechanism (Ramírez-Ochoa et al., 2022). Both BBD and PSO are extensively applied in hydrogen energy applications. Priya and Kanmani (2011) employed BBD to investigate the impact of three variable conditions on photocatalytic hydrogen production from hydrogen sulfidic in alkaline solutions. Zhao et al. (2024) assessed the effects of hydrogen doping ratio, preheating air temperature, and air factor on gas emissions from a gas boiler using the BBD method. Duan et al. (2023) utilised an enhanced PSO to analyse and predict the performance of an engine with a 20% hydrogen volume fraction. Ahmad and Yadav (2024) integrated BBD and PSO to accurately predict and optimise parameters for wastewater electrolysis in green hydrogen production. The combination of BBD and PSO improves performance and is essential for the multifactor optimisation of structural parameters. Moreover,

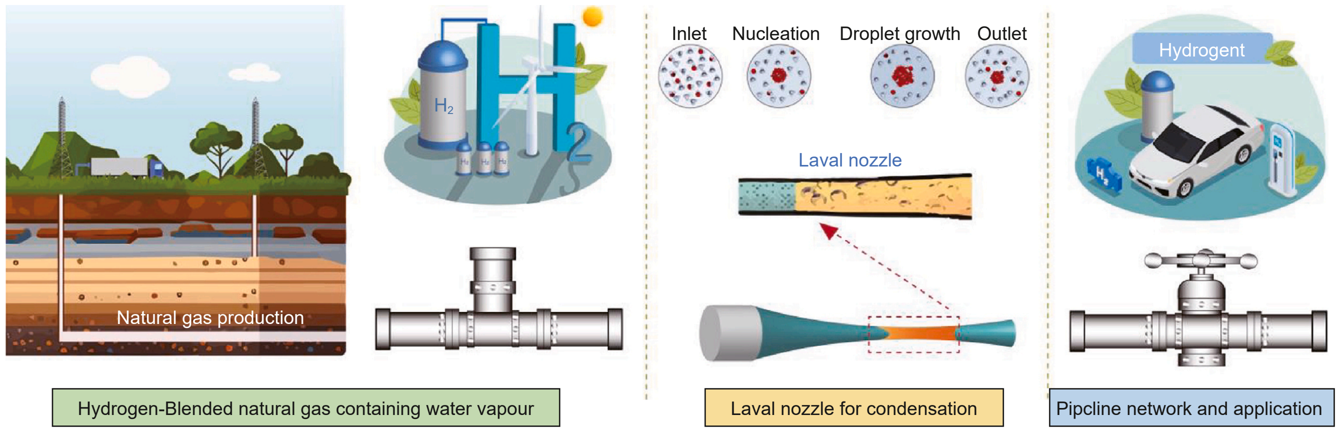

Fig. 1. Pipeline transportation flow of hydrogen-blended natural gas containing water vapour.

Table 1
Differences in the physical properties of methane and hydrogen.

Gas properties	CH_4	H_2
Relative molecular mass	16.043	2.016
Specific heat capacity	35.900	10.220
Density at 20 °C and atmospheric pressure, kg/m^3	0.660	0.083
Energy density, J/m^3	3.58×10^7	1.08×10^7
Specific gravity	0.554	0.070
Summing factor	0.045	−0.010

these optimisation techniques reduce the number of required calculations, conserving resources and time.

Currently, research on condensation in supersonic technologies involving water vapour-blended hydrogen gas is limited. Therefore, computational fluid dynamics (CFD) served as the computational platform in this study. The condensation characteristics of water-containing hydrogen-blended natural gas in Laval nozzles were calculated, and the constructed model was validated for comparison. The effect of water vapour content in hydrogen-blended natural gas on the condensation rate in Laval nozzles was investigated. This study employed BBD and PSO to examine the impact of natural gas components on water vapour condensation and to analyse how variations in CH_4, C_2H_6, C_3H_8, and H_2 contents influence the condensation process. The research aims to provide technical support for the pipeline transmission of hydrogen-blended natural gas.

2. Model

2.1. Laval nozzle geometry model

The Laval nozzle contracts and subsequently expands to produce a supersonic airflow with condensation. The Laval nozzle consists of a straight section, convergent section, throat section, and divergent section. The straight section ensures a uniform velocity distribution of water vapour containing hydrogen-blended natural gas entering the nozzle, facilitating gas contraction within the convergent section. Utilising the Witozinsky profile, the convergent section allows rapid contraction at the entrance and gradual contraction near the outlet, ensuring even gas flow distribution at the throat. Utilising the Witozinsky profile enables a smooth, non-abrupt transition from the inlet to the throat section (Wang et al., 2023). Its characteristic of continuously varying contour curvature effectively suppresses or mitigates boundary layer separation and vortex generation within the converging section (Lakzian et al., 2024). This reduces the impact of turbulence within the nozzle, enhances flow stability (Liu et al., 2023), and achieves favourable condensation effects, ensuring even gas flow distribution at the throat (Chen and Huang, 2022). The throat radius measures 8.55 mm. The divergent angle is initially set at 3.11° to enhance water vapour condensation and separation. The inlet section has a diameter of 136 mm and a length of 85 mm, while the convergent section is 238 mm long and the divergent section measures 245.4 mm. The geometry and parameters of the Laval nozzle are illustrated in Fig. 2.

The contour equations of the convergent section (Cao et al., 2021):

$$r_0 = \frac{r_{cr} + y_h}{\sqrt{1 - \left[1 - \left(\frac{r_{cr}+y_h}{r_1+y_h}\right)^2\right] \frac{\left(1-\frac{x^2}{L^2}\right)^2}{\left(1+\frac{x^2}{3\times L^2}\right)^3}}} - y_h \quad (1)$$

where y_h represents the upward and downward displacement parameter of the convergent section function, set to $y_h = 10$ mm in this model. r_{cr} denotes the throat radius of 8.55 mm, and r_1 signifies the inlet radius of 68 mm.

2.2. Mathematical models

During condensation, mass transfers from water vapour to liquid water, necessitating the inclusion of corresponding energy,

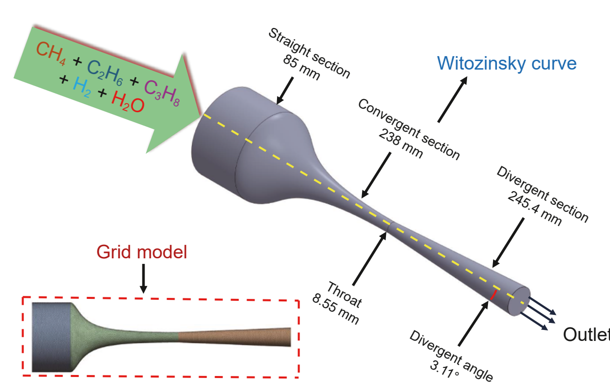

Fig. 2. Laval nozzle geometry.

momentum, and mass source terms in the control equation. The user-defined function (UDF) enables dynamic modelling of the nucleation rate alongside the mass, momentum, and energy source terms within the liquid phase. It establishes the scalar transfer framework for the liquid phase control equations using user-defined scalars (UDS).

Gas-phase control equations:

$$\frac{\partial \rho_v}{\partial t}+\frac{\partial}{\partial x_j}\left(\rho_v u_j\right)=S_m \tag{2}$$

$$\frac{\partial}{\partial t}(\rho_v u_i)+\frac{\partial}{\partial t_j}\left(\rho_v u_j u_i\right)=-\frac{\partial \rho_v}{\partial x_i}+\frac{\partial}{\partial x_j}\left[\mu\left(\frac{\partial u_j}{\partial x_i}+\frac{\partial u_i}{\partial x_j}-\frac{2}{3}\delta_{ij}\frac{\partial u_j}{\partial x_j}\right)\right]+\frac{\partial}{\partial x_j}\left(-\rho_v\overline{u_i'u_j'}\right)+S_u \tag{3}$$

$$\frac{\partial}{\partial t}(\rho_v E)+\frac{\partial}{\partial t_j}\left(\rho_v u_j E+u_j p\right)=\frac{\partial}{\partial x_j}\left(k_{\text{eff}}\frac{\partial T_v}{\partial x_j}+u_i\tau_{\text{eff}}\right)+S_h \tag{4}$$

Liquid-phase control equations:

$$\frac{\partial}{\partial t}(\rho_v Y)+\frac{\partial}{\partial x_j}\left(\rho_v u_j Y\right)=S_Y \tag{5}$$

$$\frac{\partial}{\partial t}(\rho_v N)+\frac{\partial}{\partial x_j}\left(\rho_v u_j N\right)=\rho_v J \tag{6}$$

$$r_d=\left(\frac{3Y}{4\pi\rho_l N}\right)^{\frac{1}{3}} \tag{7}$$

Droplet critical radius:

$$r_c=\frac{2\sigma}{\rho_l R_v T\ \ln S} \tag{8}$$

During condensation, the supercritical condensation nuclei form droplets, whereas subcritical and evaporating nuclei induce instability. Girshick and Chiu (1990) developed the internally consistent classical theory (ICCT) nucleation equations to address this phenomenon.

$$J=\frac{1}{S}\frac{\rho_v^2}{\rho_l}\sqrt{\frac{2\sigma}{\pi m_0^3}}\exp\left(-\frac{16\pi}{3}\frac{\sigma^3}{k_B R_M{}^2 T^3 \rho_l{}^2(\ln S)^2}\right)\exp\left(\frac{\pi a_0}{k_B T}\right) \tag{9}$$

$$a_0=(36\pi)^{\frac{1}{3}}(v_l)^{\frac{2}{3}} \tag{10}$$

Within the nozzle, the droplet radius evolves as steam molecules continuously condense, leading to a gradual enlargement of liquid droplets. The growth rate of the droplet radius is modelled using the Gyarmathy model (Gyarmathy, 1982).

$$\frac{\mathrm{d}r_{\mathrm{d}}}{\mathrm{d}t}=\frac{\lambda_v(1-r_c/r_d)(T_s-T_v)}{\rho_{\mathrm{L}}h_{\mathrm{LV}}\left(r_{\mathrm{d}}+\frac{2\sqrt{8\pi}}{1.5\ \mathrm{Pr}_v}\cdot\frac{\gamma}{\gamma+1}\bar{l}\right)} \tag{11}$$

The k–ω model is preferred for simulating compressible turbulence and wall flow within the nozzle.

$$\frac{\partial}{\partial t}(\rho_v k)+\frac{\partial}{\partial x_j}(\rho_v k u_i)=\frac{\partial}{\partial x_j}\left[\Gamma_k\frac{\partial k}{\partial x_j}\right]+G_k-Y_k \tag{12}$$

$$\frac{\partial}{\partial t}(\rho_v \omega)+\frac{\partial}{\partial x_j}(\rho_v \omega u_i)=\frac{\partial}{\partial x_j}\left[\Gamma_\omega\frac{\partial \omega}{\partial x_j}\right]+G_\omega-Y_\omega \tag{13}$$

Accurately predicting the saturated state of water vapour at different temperatures and pressures forms the physical foundation for simulating the water vapour condensation process. The PR equation can precisely describe intermolecular forces (Zhou et al., 2019). It outperforms the RK equation in predicting saturated vapour pressures and vapour-liquid phase envelopes for pure components and mixtures, offering superior accuracy in vapour-liquid equilibrium calculations (Zhou et al., 2020). This is crucial for solving condensation flow control equations coupled with mass, momentum, and energy source terms. It is widely used in engineering thermodynamics for calculating physical properties of hydrocarbon mixtures and systems containing polar components (such as water vapour). The Peng–Robinson (PR) real gas state equation is employed.

$$P_v=\frac{RT_v}{V-b}-\frac{a}{V(V+b)+b(V-b)} \tag{14}$$

Component transportation model:

$$\frac{\partial}{\partial t}(\rho_v w_i)+\frac{\partial}{\partial x_j}\left(\rho_v w_i u_j\right)=\frac{\partial}{\partial x_j}\left[\rho D_{mi}\frac{\partial w_i}{\partial x_j}\right]+S_m \tag{15}$$

To evaluate the condensation performance of the Laval nozzle, the condensation rate parameter is defined as the ratio of condensate to inlet water vapour, calculated using the corresponding equation.

$$\eta=\frac{y_{\text{in}}-y_{\text{out}}}{y_{\text{in}}}\times 100\% \tag{16}$$

2.3. Grid and independence verification

In computational fluid dynamics, grid quality and density critically affect the accuracy and convergence of results. Grid independence was confirmed using four grid sizes: sparse (8 mm, 200,843 cells), medium (6 mm, 253,429 cells), dense (4 mm, 365,385 cells), and ultra-dense (2 mm, 584,326 cells). Tetrahedral meshing was utilised for grid generation. The quantity and quality metrics for the four grid sizes are presented in Table 2. Grid skewness values between 0 and 0.25 indicate high grid quality. Additionally, cell proximity and orthogonal qualities near 1 enhance the precision of grid structure evaluations, with an excellent grid exhibiting average cell and orthogonal qualities of at least 0.7. By evaluating the skewness and right-angle quality of the grids, all four grid specifications meet the requirements. When the grid size is refined from 4 mm to the ultra-dense 2 mm, the changes in average skewness and right-angle quality are both less than 1%. Further refinement of the grid no longer significantly improves grid quality.

Table 2
Grid quality.

Grid type	Grid cells	Grid nodes	Average skewness	Right-angled mass
Sparse	200,843	55,033	0.2206	0.79832
Medium	253,429	74,684	0.2214	0.85532
Dense	365,385	106,849	0.2264	0.89517
Super-dense	584,326	119,501	0.2278	0.89673

To balance computational accuracy and efficiency, subsequent simulation analyses will adopt the “Dense” grid type.

2.4. Boundary condition settings

The Laval nozzle inlet is defined as a pressure inlet at 1 MPa and 353.15 K, whereas the outlet pressure is maintained at 0.5 MPa. The walls are assigned thermal-insulated boundary conditions. Turbulence is modelled using the standard k–ω model. To account for the compressibility of the gas, the PR real gas equation is employed. Source term and nucleation rate equations are implemented via a user-defined function. Both the component transport and volume of fluid (VOF) multiphase flow models are utilised.

2.5. Model verification

In this study, the established condensation model was validated against existing models, confirming its accuracy and reliability. The injected gas mixture composition is based on Iran’s hydrogen-blended natural gas as reported in Yan et al. (2025), with an outlet pressure of 0.5 MPa. As illustrated in Fig. 3, the model validation results align with data from Yan et al. (2025). The calculated temperature and pressure are consistent with those in reference Yan et al. (2025), thereby verifying the feasibility of the CFD approach employed in this study.

3. Algorithm optimisation

3.1. Data sources

As China’s largest oil and gas-bearing basin, the Tarim Basin’s natural gas resources display notable compositional characteristics and diverse origins. Chen et al. (2000) provides comprehensive data on the basin’s natural gas composition, which is primarily CH_4, supplemented by heavier hydrocarbons such as C_2H_6, C_3H_8, and C_4H_{10}, along with non-hydrocarbons including N_2 and CO_2. After purification, the methane (CH_4) volume content of natural gas entering the long-distance pipeline network typically exceeds 90%, often reaching 95% or higher (Ali Abd et al., 2021). Fig. 4 illustrates the components of the Tarim Basin gas fields. CH_4 is the dominant component, typically accounting for over 90% of the total natural gas. CH_4 is the dominant component, typically accounting for over 80% of the total natural gas. In some instances, methane content drops below 70%, indicating an enrichment of heavy hydrocarbons. C_2H_6 concentrations decrease with increased burial depth as methane levels rise, while the drying coefficient increases, typically ranging from 0% to 10%. The C_3H_8 and C_4H_{10} level are significantly lower, usually below 10% and often under 2%. N_2 concentrations vary widely, with certain gas fields exhibiting nitrogen levels between 18.23% and 44.59%. In regions with low to medium nitrogen natural gas, nitrogen content generally remains below 5%–10%. CO_2 levels are typically under 5%, though some fields show elevated concentrations due to carbonate rock pyrolysis or biological processes. Rare gases, such as He, are present in minimal quantities and are usually trace components of the natural gas fraction.

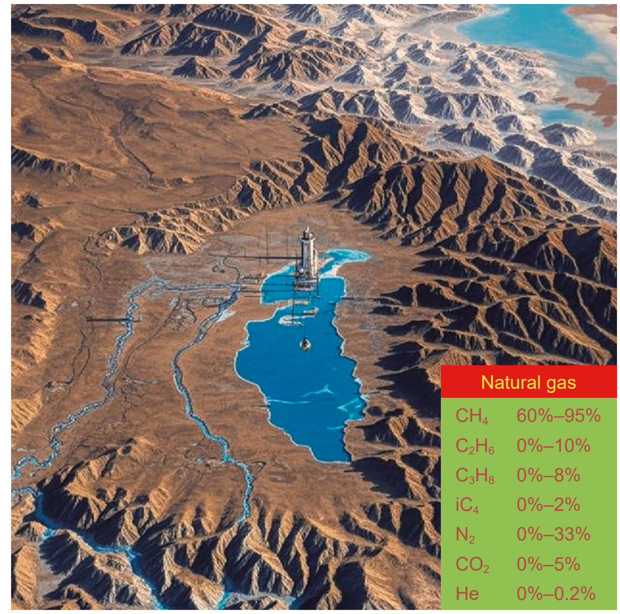

Fig. 4. Tarim Basin gas field components.

3.2. Algorithmic research framework

The Box–Behnken design is utilised as a rotating centre combination design. Condensation calculations of hydrogen-blended natural gas containing water vapour flowing through Laval

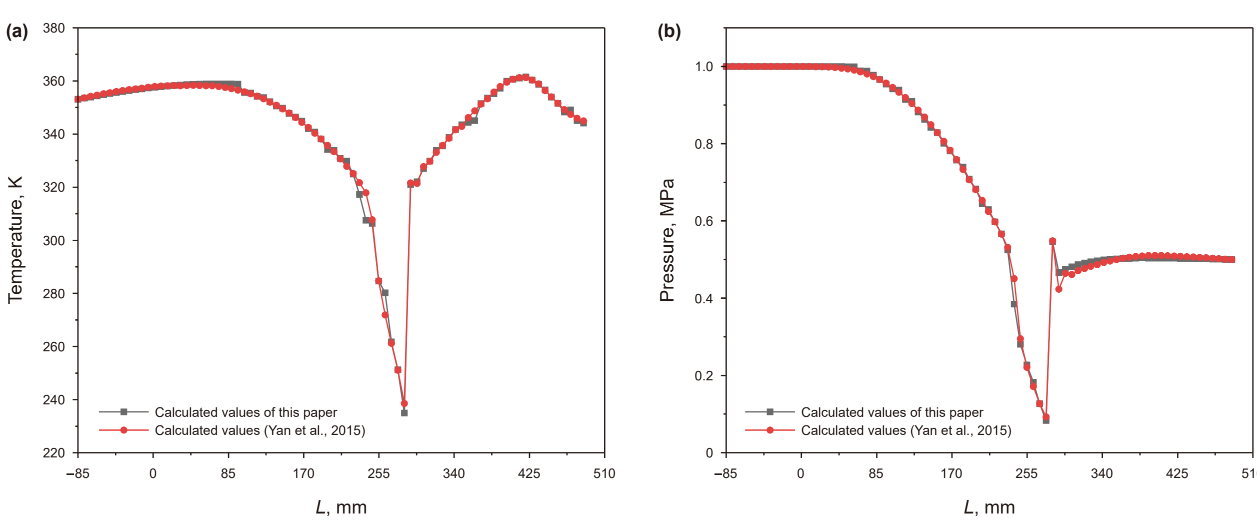

Fig. 3. Model verification. **(a)** Temperature verification. **(b)** Pressure verification.

nozzles were performed to examine the effect of gas components on Laval nozzle condensation efficiency and to develop a quadratic model. The computational effort was minimized. This study selected concentrations of CH_4, C_2H_6, C_3H_8, and H_2 as independent variables. Using BBD, the influence of gas components on water vapour condensation efficiency in Laval nozzles was analysed. A total of 29 experiments, including five central points, were randomly designed with Design-Expert (version 11.1.2.0).

PSO is an evolutionary optimisation technique that was utilised to balance local search and global exploration by tracking individuals' and groups' optimal positions. PSO assessed how natural gas components in Laval nozzles affect the condensation characteristics of hydrogen-blended natural gas with water vapour and approached the optimal solution for condensation performance. It was employed to iteratively optimise the hydrogen-blended natural gas composition, enhancing condensation rates and Laval nozzle efficiency.

By integrating BBD and PSO, computational procedures were established, variance analysis conducted, and a response surface model developed. The response surface regression model's extreme points and their optimal independent variable combinations were identified. Finally, the PSO-derived optimal solution was validated through CFD simulations. This study investigates the condensation of hydrogen-blended natural gas containing water vapour within a Laval nozzle, as depicted in Fig. 5.

3.3. BBD model

Natural gas is a mixture of hydrocarbons, which exhibits a complex composition significantly influenced by geological conditions, genesis types, and development processes. Due to varying components and concentrations, this research specifically examines the effect of hydrocarbon gases on water vapour condensation. When conducting a BBD experimental design using Design-Expert software, N_2 is set as the purge gas. When generating 29 experimental plans, the sum of concentrations for all specified variables (CH_4, C_2H_6, C_3H_8, H_2) and N_2 is 100%. Several pipeline hydrogens blending demonstration projects are currently underway globally. Examples include the EU's "HyBlend" project and China's "Ningdong Natural Gas Hydrogen Blending Pipeline Demonstration Project." Typically, hydrogen volume fractions below 20% are considered compatible with existing infrastructure. CH_4 concentrations were set at three levels-60%, 70%, and 80%-covering scenarios ranging from heavy hydrocarbon-rich to typical natural gas compositions. H_2 concentrations were set at 5%, 12.5%, and 15%, encompassing typical scenarios from preliminary exploration to higher blending ratios. The concentrations of CH_4, C_2H_6, C_3H_8, and H_2 were selected as independent variables, with N_2 comprising the remaining gas. The BBD was employed to determine the number of simulation groups, assigning each of the four variables to three levels: low (−1), medium (0), and high (+1), as listed in Table 3.

Table 3
Levels of independent variables and responses.

Level	CH_4	C_2H_6	C_3H_8	H_2
−1	60%	0%	0%	5%
0	70%	2%	1%	12.5%
+1	80%	4%	2%	15%

As presented in Table 4, 29 simulation groups were established, and the condensation rate for each was calculated using CFD. Groups 20, 21, 23, 27, and 29 represent central composite models. Intermediate-level calculations were repeated to estimate errors, enhance model accuracy, and mitigate random errors. The condensation rates across the 29 groups ranged from 71% to 79%. The highest condensation rate of 78.65% was observed in group 23, whereas the lowest rate of 71.342% occurred in group 11.

The interactions between natural gas components and water vapour affect condensation characteristics; therefore, the analysis of variance (ANOVA) is presented in Table 5. The *F*-value

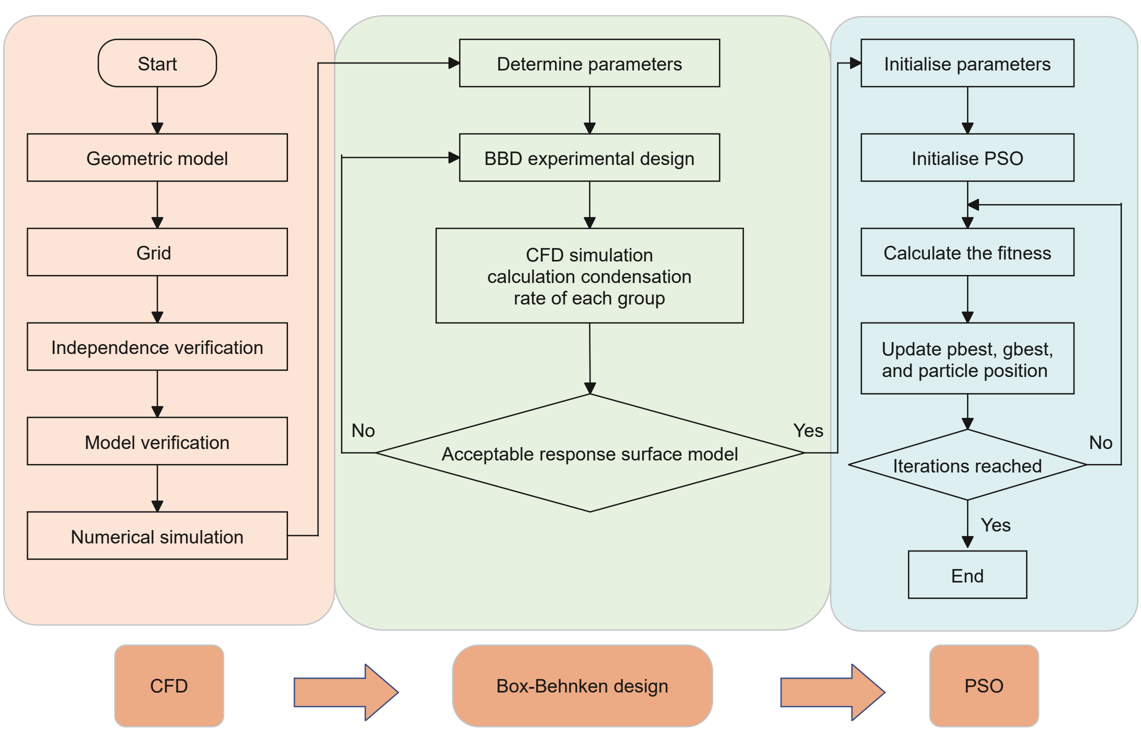

Fig. 5. CFD-BBD-PSO process.

Table 4
BBD and condensation rate results.

Groups	CH_4, %	C_2H_6, %	C_3H_8, %	H_2, %	N_2, %	Total, %	Condensation rate, %
1	70	0	1	5	24	100	76.153
2	80	2	1	15	2	100	75.166
3	60	0	1	10	29	100	76.603
4	80	2	2	10	6	100	75.476
5	70	2	0	5	23	100	74.84
6	60	2	1	15	22	100	73.945
7	70	2	2	5	21	100	74.126
8	70	4	1	15	10	100	74.596
9	70	4	2	10	14	100	76.168
10	70	0	2	10	18	100	74.649
11	70	2	0	15	13	100	71.342
12	70	0	1	15	14	100	75.084
13	80	2	1	5	12	100	76.226
14	60	2	1	5	32	100	76.411
15	70	2	2	15	11	100	74.138
16	60	4	1	10	25	100	76.047
17	70	4	0	10	16	100	73.076
18	70	4	1	5	20	100	76.346
19	70	0	0	10	20	100	74.102
20	70	2	1	10	17	100	77.85
21	70	2	1	10	17	100	78.12
22	60	2	2	10	26	100	76.081
23	70	2	1	10	17	100	78.65
24	60	2	0	10	28	100	74.686
25	80	0	1	10	9	100	76.355
26	80	2	0	10	8	100	73.742
27	70	2	1	10	17	100	78.57
28	80	4	1	10	5	100	75.846
29	70	2	1	10	17	100	78.35

assesses each factor's effect on the model's response variable and determines its significance. The *P*-value evaluates the statistical significance of each factor's influence on the response variable, with values above 0.05 typically considered non-significant. The analysis identified a significant impact on the coagulation rate ($P < 0.05$), highlighting C_3H_8 and H_2 as key factors. These findings suggest that the developed regression model sufficiently fits and captures the influence of the examined factors on the condensation rate, establishing a basis for further studies on the effects of natural gas components on water vapour condensation.

Based on the fitting analysis of simulation results using the BBD, the obtained response aligns with the quadratic equation describing the condensation effect:

$$Y = 78.31 - 0.0802 \times A - 0.0723 \times B + 0.7375 \times C - 0.8193 \times D + 0.0118 \times A \times B + 0.0847 \times A \times C + 0.3515 \times A \times D + 0.6363 \times B \times C - 0.1702 \times B \times D + 0.8775 \times C \times D - 0.8812 \times A^2 - 1.08 \times B^2 - 2.65 \times C^2 - 1.91 \times D^2 \tag{17}$$

3.4. PSO

This study investigates the impact of natural gas components on the condensation rate employing PSO, with CH_4, C_2H_6, C_3H_8, and H_2 as particles. The positions and velocities of the particle swarm were initialised randomly, and the optimal solution was achieved through iterative optimisation. In each iteration, particles adjust their positions by referencing their personal best (p_{best}) and the global best (g_{best}) extrema. Initial fitness values are computed, and both individual and global optima are recorded.

Velocity equation:

$$v_i^{(t+1)} = \omega v_i^{(t)} + c_1 r_1 \times \left(p_{\text{best}_i}^{(t)} - x_i^{(t)}\right) + c_2 r_2 \times \left(g_{\text{best}_i}^{(t)} - x_i^{(t)}\right) \tag{18}$$

$$x_i^{(t+1)} = x_i^{(t)} + v_i^{(t+1)} \tag{19}$$

$$\omega^{(t)} = \omega_{\max} - \frac{\omega_{\max} - \omega_{\min}}{T_{\max}} \times t \tag{20}$$

In the governing equation, r_1 and r_2 are independent random variables uniformly distributed between 0 and 1. Here, x_i denotes the current position, and v_i represents the velocity of the particle. The learning factors c_1 and c_2 are typically set to 2. The inertia weight ω manages the balance between global exploration and local exploitation in PSO, often utilising a linearly decreasing strategy.

As particles move, their extreme values are promptly updated. Additionally, the algorithm evaluates the fitness $f(x)$ of the new position of each particle.

Update the individual optimal equation:

Table 5
Analysis of variance.

Source	Sum of squares	Mean squares	*F*-value	*P*-value	Significance
Model	79.87	5.71	31.12	<0.0001	Significant
A	0.0771	0.0771	0.4207	0.5271	
B	0.0626	0.0626	0.3417	0.5681	
C	6.53	6.53	35.61	<0.0001	
D	8.05	8.05	43.94	<0.0001	
AB	0.0006	0.0006	0.003	0.9571	
AC	0.0287	0.0287	0.1567	0.6981	
AD	0.4942	0.4942	2.7	0.1229	
BC	1.62	1.62	8.83	0.0101	
BD	0.1159	0.1159	0.6325	0.4397	
CD	3.08	3.08	16.8	0.0011	
A^2	5.04	5.04	27.48	0.0001	
B^2	7.51	7.51	40.97	<0.0001	
C^2	45.58	45.58	248.67	<0.0001	
D^2	23.6	23.6	128.76	<0.0001	
Residual	2.57	0.1833			
Lack of fit	2.13	0.2134	1.97	0.2677	Not significant
Pure error	0.4325	0.1081			
Cor total	82.44				

Note: Model A is CH_4, Model B is C_2, Model C is C_3, Model D is H_2.

$$p_{\text{best}_i}^{(t+1)} = \left\{p_{\text{best}_i}^{(t)},\ \text{otherwise}\ x_i^{(t+1)},\ \text{if}\ f\left(x_i^{(t+1)}\right) < f\left(p_{\text{best}_i}^{(t)}\right)\right. \quad (21)$$

Update the global optimal equation:

$$g_{\text{best}}^{(t+1)} = \underset{i}{\operatorname{argmin}} f\left(p_{\text{best}_t}^{(t+1)}\right) \quad (22)$$

Upon initialisation, the particle swarm size P_1 is set to 29, and the dimensionality D is 4. The number of iterations N_i is configured to 200. The search space boundaries, $x_{\min}$ and $x_{\max}$, are determined based on the specified constraints. The initial swarm is randomly generated within the design space [$x_{\min}$, $x_{\max}$], with the velocity components v_{ji} and position vectors x_{ji} of each particle assigned randomly.

$$v_i^j = v_{\min} + r_1(v_{\max} - v_{\min}) \quad (23)$$

$$x_i^j = x_{\min} + r_2(x_{\max} - x_{\min}) \quad (24)$$

In this context, v_{ji} and x_{ji} denote the velocity and position components of particle i along the j-th dimension, where i ranges from 1 to 29 and j from 1 to 4. The stochastic parameters r_1 and r_2 are drawn from a uniform distribution over the interval [0,1]. Velocity constraints are imposed using predefined limits $v_{\max}$ and $v_{\min}$, representing the upper and lower bounds for particle velocities.

During the particle velocity and position update phase, the iterative process is assessed against the predefined termination criteria. If the termination condition remains unmet, the fitness function of each particle is re-evaluated to guide subsequent optimisation steps. Conversely, upon meeting the termination criteria, the final fitness value is output and recorded as the optimal solution to the optimisation problem.

3.5. BBD-PSO results

Owing to the relatively high proportion of CH_4 in natural gas, the response surface regression model was developed using BBD. CH_4 and the other three gases directly influence water vapour condensation visualization. Each figure includes two independent variables, while the remaining factors are held constant at their central values. Fig. 6 presents the three corresponding response surface diagrams, which display clear bending characteristics. The response surfaces curve downward, indicating that CH_4 and the three gases achieve a maximum value for water vapour condensation. The contour shapes are elliptic, signifying significant interactions between the gases.

The global optimal value of the response surface regression model was determined using PSO. Table 6 presents the optimal solutions swiftly obtained using PSO by calculating the relevant setting parameters. Consequently, the post-optimisation absolute values indicate the optimal setting rates, with the optimal values determined through iterations.

Table 7 summarizes the BBD–PSO calculation results, showing that the gas composition consists of 69.212% CH_4, 2.028% C_2H_6, 1.107% C_3H_8, and 9.01% H_2. This mixture maximizes the water vapour condensation efficiency of hydrogen-blended natural gas flowing through Laval nozzles.

4. Results and discussion

The four gases CH_4, C_2H_6, C_3H_8, and H_2 significantly affect water vapour condensation. BBD–PSO calculated the optimal gas composition to achieve maximum water vapour condensation. Three reference groups with engineering and physical significance were established. The first group contained only CH_4 and H_2, with N_2 as the filler gas. The second group represented a common ternary mixture. Building upon the first group, C_2H_6 was added to simulate common hydrogen-blended natural gas containing ethane but no propane, serving as a benchmark closer to certain practical scenarios. The third group comprises CH_4 (70%), C_2H_6 (2%), C_3H_8 (1%), and H_2 (12.5%), representing the central level values for each component set in the BBD design. This group represents a design prior to fine-tuning via the PSO algorithm. The variations in pressure, temperature, subcooling degree, Mach number, droplet mass fraction, and droplet radius within Laval nozzles are examined. These flow field factors influence the water vapour condensation rate. Analysis of the results shows that for the first group composition, the condensed droplet radius was smaller, and the liquid mass fraction at the nozzle outlet was the lowest at 2.327%. For the second group with hydrogen-blended natural gas components, the liquid mass fraction at the nozzle outlet was 2.627%, representing a 12.89% increase over the first group. The liquid mass fraction at the nozzle outlet for the hydrogen-blended natural gas composition in the third group was

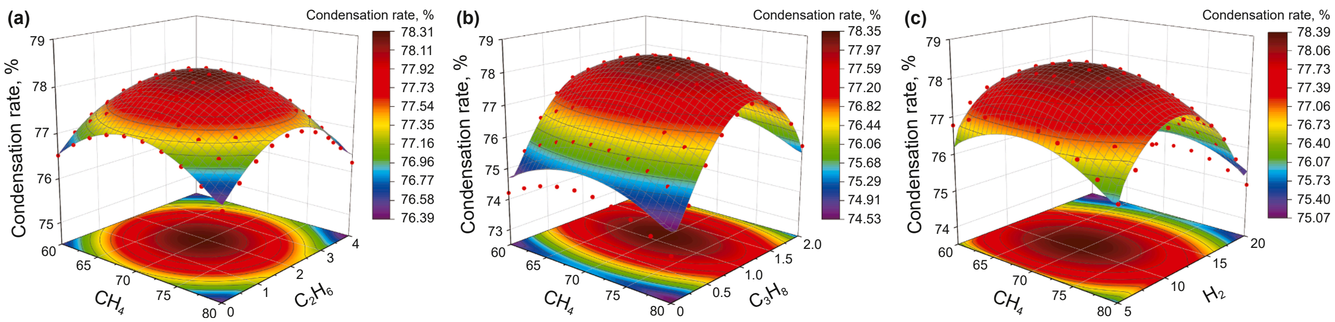

Fig. 6. Response surface diagram. (**a**) CH_4 and C_2H_6. (**b**) CH_4 and C_3H_8. (**c**) CH_4 and H_2.

Table 6
PSO parameter settings.

Parameters	Meaning	Setting
ω	Inertia weight	0.7
c_1	Individual learning factor	2
c_2	Social learning factor	2
N	Particle swarm size	29
D	Particle swarm dimension	4

Table 7
Optimal solution of gas parameters.

Gas	CH_4	C_2H_6	C_3H_8	H_2	Condensation rate
Gas content	69.212%	2.028%	1.107%	9.01%	78.65%

2.776%, representing an increase of approximately 19.3% compared to the first group. The optimal group achieved a liquid mass fraction of 3.08% at the nozzle outlet, marking an increase of approximately 32.36% over the first group and the largest improvement rate.

4.1. Pressure

The pressure of hydrogen-blended natural gas with different components varies at various points within the Laval nozzle, as illustrated in Fig. 7, which includes the pressure distribution (Fig. 7(a)) and pressure along the central axis (Fig. 7(b)). Fig. 7(a) depicts the characteristic variations in pressure distribution across different sections of the Laval nozzle. In the inlet region, pressure remains relatively stable. As the flow enters the convergent section, pressure steadily decreases due to the continuous reduction in the pipe's cross-sectional area. Within the divergent section, despite the increased gas expansion from the gradual widening of the pipe diameter, pressure inversely rises. At the throat, pressure sharply drops and then rebounds over a short distance. Fig. 7(b) illustrates the central axis pressure of the Laval nozzle, which initially decreases and then increases. Due to variations in hydrogen-blended natural gas components, the density of the mixtures differs. When density changes, the mass flow rate alters under identical inlet pressure and nozzle inlet area conditions. Changes in mass flow rate affect the flow field distribution within the nozzle. Increased flow alters the acceleration and expansion processes of hydrogen-blended natural gas within the nozzle, consequently influencing shock wave position and intensity. Changes in flow rate indirectly affect shock wave intensity by altering the velocity and temperature of hydrogen-blended natural gas within the nozzle. Flow variations also indirectly influence shock wave strength through associated changes in velocity and temperature. For the four hydrogen-blended natural gas compositions, shock wave locations along the nozzle axis were measured at 269, 276, 283, and 283 mm, respectively. From −85 mm to 60 mm within the nozzle, pressure remains largely unchanged. Between 110 mm and near the rear of the throat, pressure gradually decreases. From 262 mm to the minimum pressure of 0.18 MPa, only CH_4 and H_2 are present. The pressures of components containing CH_4, H_2, C_2H_6, C_3H_8, and PSO optimisation decrease to minima of 0.21 MPa and 0.19 MPa at 269 mm, with only

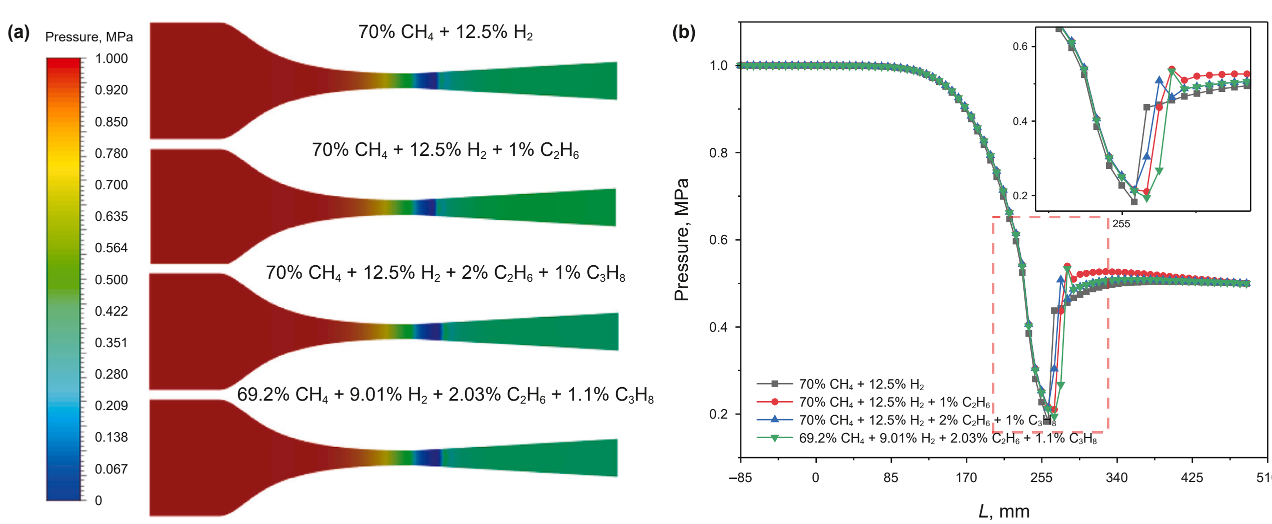

Fig. 7. Pressure inside the Laval nozzle. (**a**) Pressure distribution. (**b**) The pressure on the central axis.

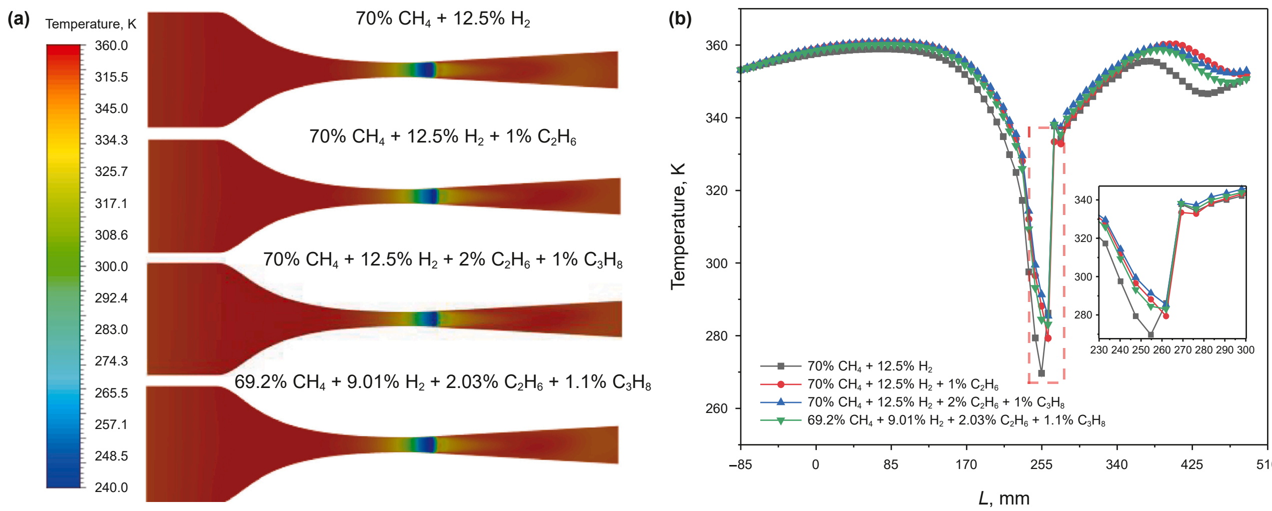

Fig. 8. Temperature inside the Laval nozzle. **(a)** Temperature distribution. **(b)** Temperature along the central axis.

CH_4 and H_2 remaining. Between 262 mm and 269 mm, pressure suddenly increases to 0.43 MPa, and subsequently, pressure in the divergent section continues to rise, approaching 0.5 MPa. The optimised components—CH_4, H_2, C_2H_6, C_3H_8, and PSO—experienced a sudden pressure increase to 0.53 MPa between 269 and 283 mm, subsequently stabilizing near 0.5 MPa within the divergent section.

4.2. Temperature

The temperature of hydrogen-blended natural gas, comprising varying components, varies across different regions of the Laval nozzle. Fig. 8 depicts the temperature distribution inside the Laval nozzle (Fig. 8(a)) and along its central axis (Fig. 8(b)). As shown in Fig. 8(a), the internal temperature field displays distinct features: in the inlet and convergent sections, the airflow temperature ranges from 348 to 360 K. Progressing into the latter half of the convergent section toward the throat, the temperature decreases, reaching approximately 260 K near the throat. Upon entering the divergent section, the temperature progressively rises, returning to 360 K near the nozzle outlet. Fig. 8(b) illustrates the temperature profile along the nozzle's central axis, exhibiting an initial decline followed by a gradual recovery. For mixtures containing only CH_4 and H_2 from 83 to 255 mm, the temperature sharply decreases to 269.67 K. The lowest temperatures along the nozzle axis for the four hydrogen-blended natural gas mixtures were recorded at 254.7, 261.9, 262.3, and 262.93 mm, respectively. In contrast, mixtures optimised by PSO, containing CH_4, H_2, C_2H_6, and C_3H_8 from 83 mm to 261 mm, exhibit temperature reductions to 279.3, 285, and 283.5 K, respectively. Condensation of water vapour commences at approximately 263 mm. As the vapour transforms into small droplets, it releases heat, leading to a temperature rise within the divergent section. The gas mixture consists solely of CH_4, H_2, and C_2H_6. From 274 mm to the outlet, the temperature continues to increase, reaching 335 K, while the other three components rise to 238 K. This temperature elevation in the divergent section is attributed to the reverse evaporation of condensed water vapour, significantly diminishing the coagulation efficiency of the Laval nozzle.

4.3. Mach number

The gas flow velocity in a Laval nozzle is high and is typically characterized by the Mach number to describe its high-speed flow properties. The Mach numbers of different components in hydrogen-blended natural gas vary along the length of the Laval nozzle. As illustrated in Fig. 9, the Mach number distribution of hydrogen gas containing water vapour within the Laval nozzle is shown in Fig. 9(a), and the Mach number along the central axis is depicted in Fig. 9(b). In Fig. 9(a), the gas maintains a steady flow rate in the inlet section. As the airflow enters the convergent section with a tapered design, the velocity gradient of the gas flow increases. According to the Bernoulli equation, static air pressure is continuously converted into kinetic energy, resulting in an increasing Mach number. Upon entering the divergent section, the Mach number begins to decline, ultimately establishing a specific supersonic airflow distribution at the nozzle outlet. Fig. 9(b) depicts the variation of the Mach number along the central axis of the Laval nozzle, showing an initial increase followed by a subsequent decrease. In the region from −85 to 60 mm, the Mach number remains relatively constant. As the flow approaches the throat beyond 85 mm, the Mach number gradually increases. Specifically, only CH_4 and H_2 achieve a peak Mach number of 1.41 at 261 mm, while the other three groups reach a maximum of 1.36 at 263 mm. The locations with the highest Mach number along the nozzle axis for the four hydrogen-blended natural gas mixtures are 261, 269.1, 261.9, and 261.9 mm, respectively. Between 261 and 369 mm, where only CH_4 and H_2 are present, the Mach number decreases to 0.84 and continues to decline to 0.21 at the outlet. In Laval nozzles containing CH_4, H_2, and C_2H_6, the Mach number sharply drops to 0.54 between 263 and 283 mm. For mixtures comprising CH_4, H_2, C_2H_6, C_3H_8, and PSO-optimised fractions, the Mach number decreases sharply to 0.65 from 263 to 276 mm, followed by a gradual reduction to approximately 0.21 at the outlet.

4.4. Degree of supercooling

The degree of supercooling denotes the temperature difference between the actual gas temperature and its theoretical freezing point during the cooling process. Fig. 10 illustrates the distribution of supercooling degrees in hydrogen-blended natural gas with varying components both within the Laval nozzle (Fig. 10(a)) and along the central axis (Fig. 10(b)). Notably, Fig. 10(a) indicates that within the straight pipe and the convergent section, the degree of supercooling remains below 0 K. As air traverses the convergent section of a Laval nozzle, the supercooling parameter continuously increases. Near the nozzle's throat—the minimum section—the

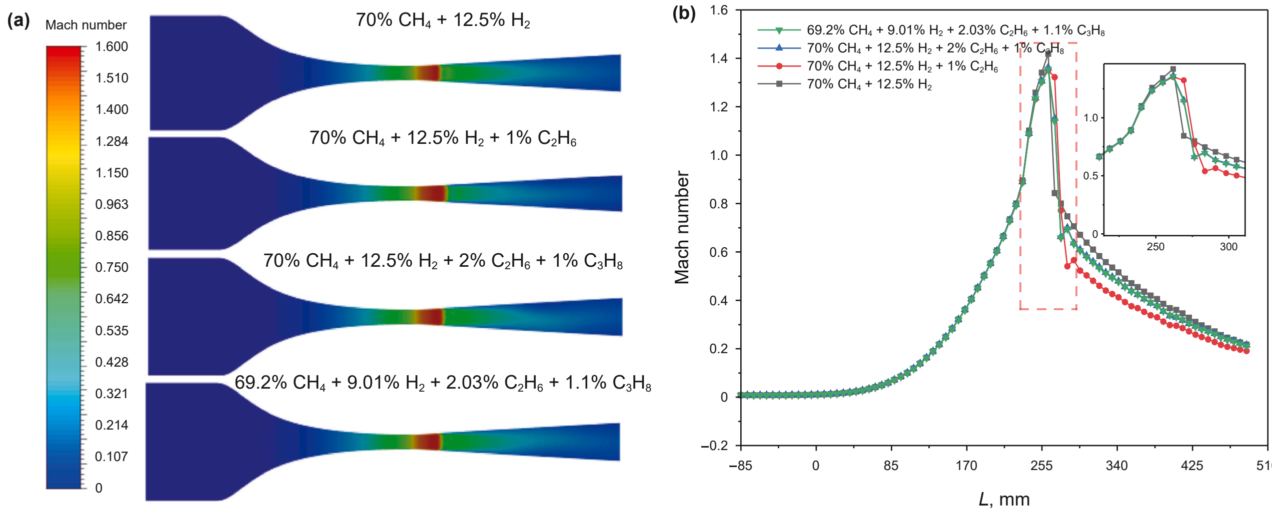

Fig. 9. Mach number inside the Laval nozzle. (**a**) Mach number distribution. (**b**) Mach number on the central axis.

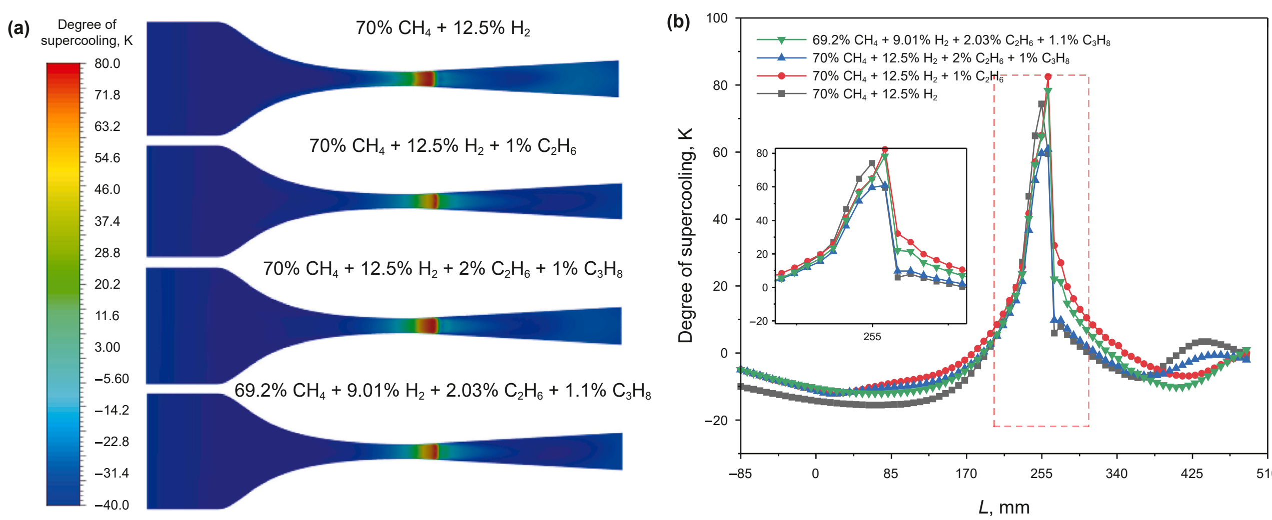

Fig. 10. Degree of undercooling. (**a**) Degree of supercooling. (**b**) Degree of subcooling along the central axis.

supercooling degree reaches an extreme, leading to the phase change condensation of water vapour. Upon entering the divergent section, the undercooling degree rises again. Fig. 10(b) illustrates that the subcooling degree along the Laval nozzle's central axis initially increases and then decreases. Within the −85 to 85 mm region of the nozzle, the supercooling degree exhibits minor fluctuations, generally remaining below 0 K. Approaching 85 mm to the throat, the supercooling degree increases. Specifically, a Laval nozzle containing only CH_4, H_2, and C_2H_6 achieves a maximum supercooling of 82.5 K at 262 mm, while a nozzle with only CH_4 and H_2 reaches a maximum of 74 K at 254 mm. PSO-optimised components in the Laval nozzle attain a peak supercooling degree of 78 K at 262 mm. From the throat to the nozzle's end, the supercooling degree steadily decreases to 0 K.

4.5. Liquid mass fraction

The liquid mass fraction of hydrogen-blended natural gas significantly varies with different components. When the gas inside the nozzle rapidly expands and its temperature drops below the saturation temperature, spontaneous condensation forms tiny droplets. In the nozzle expansion section, the gas temperature rebounds after a sharp drop near the throat. When the degree of supercooling at the throat and the leading edge of the expansion section reaches a critical value, water vapour condenses, releasing a large amount of latent heat. This heat is absorbed by the surrounding gas, causing a local temperature increase. Additionally, shock waves generated within the mixture due to back pressure and wall friction cause a sudden drop in flow velocity, converting part of the kinetic energy into internal energy. These factors are the primary drivers of the temperature rebound. When the local temperature in the expansion section rises above the saturation temperature of water vapour at the current pressure, some of the formed condensation nuclei undergo re-evaporation. This process consumes latent heat, thereby suppressing further local temperature increases. As shown in Fig. 11, the liquid mass fraction distribution of the Laval nozzle is depicted in Fig. 11(a), and the liquid mass fraction along the central axis is presented in Fig. 11(b). Fig. 11(a) shows that water vapour primarily begins to condense downstream of the throat. In the divergent section of the Laval nozzle, the main airflow accelerates droplets, resulting in a liquid mass fraction of up to 0.03. Fig. 11(b) presents line graphs of the

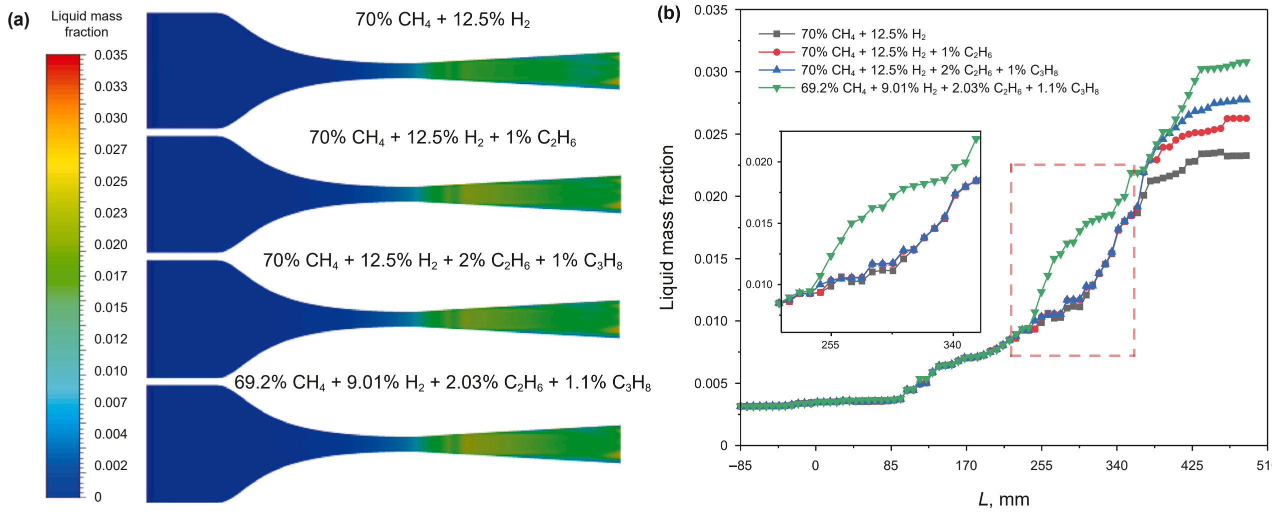

Fig. 11. Liquid mass fraction. **(a)** Liquid mass fraction. **(b)** Droplet mass fraction on the central axis.

liquid mass fraction for four models along the Laval nozzle axis, clearly indicating that the liquid mass fraction steadily increases from the inlet to the divergent section, reaching its peak at the outlet. Due to variations in hydrogen-blended natural gas components, the liquid mass fraction and water vapour condensation rate differ. The liquid mass fraction at the outlet reaches its maximum for all four hydrogen-blended natural gas components. The component with the highest liquid mass fraction at the axial outlet is the algorithmically optimised hydrogen-blended natural gas, with a liquid mass fraction of 3.08%. The lowest liquid mass fraction was observed for the CH_4–H_2 hydrogen-blended natural gas mixture, with an outlet liquid mass fraction of 2.33%. This spatial variation stems from differences in gas composition and a slight lag effect in the release of latent heat of condensation. The PSO-optimised model achieves a mass fraction at the outlet that surpasses the other models, attaining up to 0.03. Near the throat, the coagulation efficiency of the PSO-optimised components is markedly higher than that of the other three models. Models containing CH_4, H_2, C_2H_6, and C_3H_8 exhibit a higher liquid mass fraction compared to those with only CH_4, H_2, and C_2H_6 or just CH_4 and H_2. Both C_2H_6 and C_3H_8 enhance the condensation of water vapour.

4.6. Droplet radius

During condensation, numerous water vapour molecules form nuclei, leading to increased droplet radii. Fig. 12 illustrates the droplet radius distribution within the Laval nozzle (Fig. 12(a)) and along the central axis (Fig. 12(b)). Droplet radii initially grow before slightly decreasing. Larger droplets predominantly accumulate near the divergent section and along the pipe wall of the Laval nozzle. Within the Laval nozzle, droplet evaporation reduces droplet diameter downstream of the temperature region. As illustrated in Fig. 12(b), the droplet radius along the nozzle's central axis increases at the throat before decreasing in the divergent section. The PSO-optimised mixtures display the largest droplet radius at the throat, reaching 0.59 μm for CH_4 and H_2 mixtures and up to 0.553 μm for those containing CH_4, H_2, and C_2H_6. The model comprising CH_4, H_2, C_2H_6, and C_3H_8 achieves a maximum droplet radius of 0.563 μm at the throat. Near the throat, where temperatures are lowest, the droplet radius increases more rapidly. In the divergent section, temperatures rise, and the droplet radius decreases. These results indicate that the PSO-optimised model effectively enhances the condensate behaviour of hydrogen-blended natural gas.

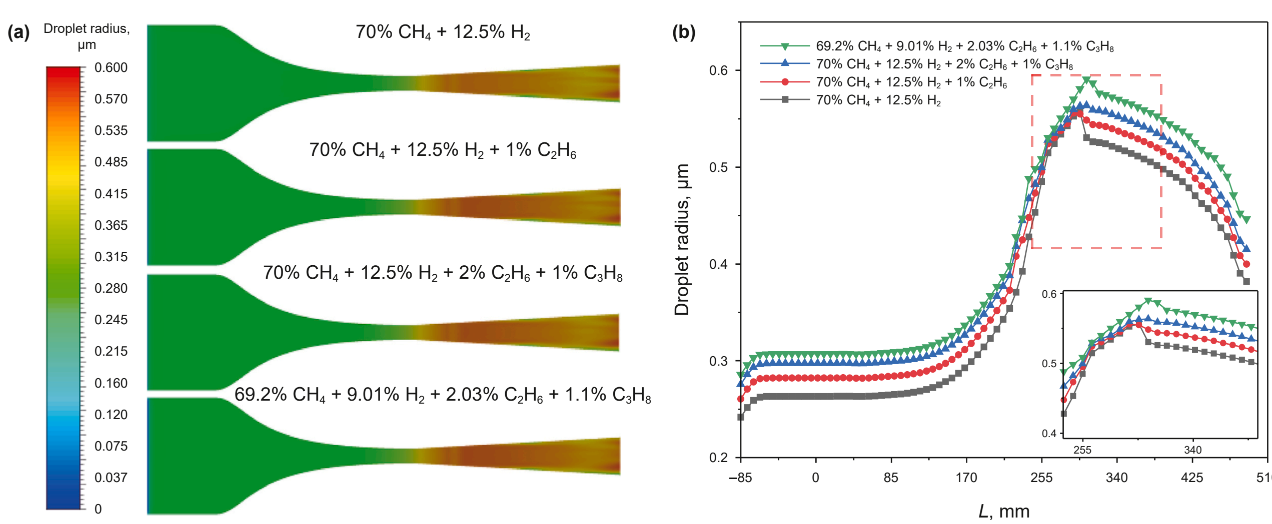

Fig. 12. Droplet radius. **(a)** Droplet radius distribution. **(b)** Droplet radius along the central axis.

5. Conclusions

This study presents a computational investigation of the phase change behaviour of hydrogen-blended natural gas containing water vapour within a Laval nozzle geometry. Utilising BBD and PSO, the influence of natural gas components on water vapour condensation efficiency was explored, leading to improved condensation performance. Compared to four groups with varying gas compositions, pressure, temperature, Mach number, degree of supercooling, liquid mass fraction, and droplet radius all exhibited changes in the condensation rate. The key conclusions are listed below:

(1) Hydrogen-blended natural gas containing water vapour was introduced into the Laval nozzle at a consistent flow rate. In the convergent section, where the nozzle diameter narrows and hydrogen gas pressure is present, the temperature decreased while the velocity gradually increased. Near the throat, the temperature fell to approximately 260 K, creating conditions favourable for the condensation of water vapour mixed with hydrogen gas.
(2) Water vapour in the hydrogen-blended natural gas spontaneously condensed near the throat, where water vapour molecules coalesced to form small droplets, increasing their radii. As the temperature rose in the divergent section, these water droplets evaporated back into vapour, resulting in smaller droplet radii and reduced water content.
(3) The various components and their concentrations in hydrogen-blended natural gas influenced the condensation efficiency of water vapour within Laval nozzles. The condensation efficiency of CH_4, H_2, C_2H_6, and C_3H_8 was significantly higher compared to mixtures containing only CH_4 and H_2 or combinations of CH_4, H_2, and C_2H_6.
(4) Utilising BBD and PSO to explore different compositions and concentrations of hydrogen-blended natural gas demonstrated that CH_4, H_2, C_2H_6, and C_3H_8 concentrations of 69.212%, 2.028%, 1.107%, and 9.01%, respectively, achieved a condensation rate of 78.65% through the Laval nozzle. The condensation rate of hydrogen-blended natural gas components was significantly enhanced following optimisation.

CRediT authorship contribution statement

Guan-Wei Jia: Writing – original draft, Software, Investigation, Funding acquisition, Conceptualization. **Kai-Feng Xue:** Writing – original draft, Software, Investigation. **Rui Li:** Writing – review & editing, Supervision, Funding acquisition, Conceptualization.

Data availability

Data will be made available on request.

Declaration of competing interest

The authors declare that they have no known competing financial interests or personal relationships that could have appeared to influence the work reported in this paper.

Acknowledgements

This work was supported by Advanced Energy Storage Materials Joint Fund Program of Kaifeng, China (No. 2407006), Science and Technology Development Project of Henan Province (No. 252102240079), National Key Research and Development Program of China (No. 2022YFB3207600 and No. 2022YFC3070100), and Fundamental Research Funds for the Central Universities.

Nomenclature

r_0	Radius of any cross-section of convergent section, mm
x	Distance from any cross-section to the inlet, mm
r_1	Nozzle inlet radius, mm
r_{cr}	Throat radius, mm
L	Convergence segment length, mm
ρ_v	Density of the vapour, kg· m^{-3}
t	Time, s
u_i	Velocity in x-axis component, m· s^{-1}
u_j	Velocity in y-axis component, m· s^{-1}
S_m	Source term in continuity equation, kg· m^{-3}· s^{-1}
S_u	Source term in momentum equation, kg ·m^{-2}· s^{-2}
S_h	Source term in energy equation, J· m^{-3}· s^{-1}
Γ_k	Effective rate of dissipation of turbulent kinetic energy
Γ_ω	Dissipation rate of turbulent kinetic energy
G_k	The turbulent kinetic energy under the condition of average velocity gradient
G_ω	The dissipation rate under the condition of average velocity gradient
Y_k	The dissipation of k under the turbulent state
Y_ω	The dissipation of ω under the turbulent state
μ	Dynamic viscosity, Pa·s
δ_{ij}	Kronecker symbol
V	Gas molar volume, m^3· mol^{-1}
E	Total energy, J· kg^{-1}
k_{eff}	Effective thermal conductivity, W·m^{-1}· K^{-1}
τ_{eff}	Effective stress tensor
Y	Liquid mass fraction
S_Y	Source term of liquid continuity equation, kg·m^{-3}·s^{-1}
N	Droplet number density, kg^{-1}
J	Nucleation rate, m^{-3}·s^{-1}
r_d	Droplet radius, m
ρ_L	Liquid density, kg·m^{-3}
σ	Droplet surface tension, N·m^{-1}
S	Supersaturation
R_v	Real gas constant, J·kg^{-1}·mol^{-1}
a	Energy parameter
b	Size parameter
ζ	Empirical coefficient
λv	Thermal conductivity of the vapour, W·m^{-1}·K^{-1}
a_0	Molecular surface area, m^2
m_v	Molecular weight, kg
k_B	Boltzmann'f''s constant, 1.3806 × 10^{-23} J· K^{-1}
r_c	Critical radius of a liquid droplet, m
T_s	Saturation temperature, K
T_v	Gas temperature, K
P_r	Prandtl number
h_{Lv}	Latent heat of condensation, J·kg^{-1}
γ	Heat ratio
Kn	Knudsen number
W_i	Mass fraction of species *i*
D_{mi}	Diffusion coefficient of substance *i* in the mixture
$\bar{l}$	Molecular mean free range
R	gas constant, 8.314 J· mol^{-1}·K^{-1}
Y_h	Convergent function up and down displacement parameter
α	Divergent angle
L_d	Divergent length
g_{best}	Global optimum
p_{best}	Individual optimum

x_i	The current position of the particle
v_i	The velocity of particles
c	Learning factor
r	Random number
ω	Inertia weight
N	Particle swarm size
D	Particle swarm dimension
T	Temperature, K
N_i	Number of iterations
c_1	Individual learning factor
c_2	Social learning factor

Abbreviations

BBD	Box–Behnken design
PSO	Particle swarm optimisation
CFD	Computational fluid dynamics
UDF	User-defined function
UDS	Using user-defined scalars
VOF	Volume of fluid
ANOVA	Analysis of variance
PR	Peng–Robinson

References

Abdin, Z., 2024. Bridging the energy future: the role and potential of hydrogen co-firing with natural gas. J. Clean. Prod. 436, 140724. https://doi.org/10.1016/j.jclepro.2024.140724.

Acar, C., Dincer, I., 2019. Review and evaluation of hydrogen production options for better environment. J. Clean. Prod. 218, 835–849. https://doi.org/10.1016/j.jclepro.2019.02.046.

Ahmad, A., Yadav, A.K., 2024. Parametric analysis of wastewater electrolysis for green hydrogen production: A combined RSM, genetic algorithm, and particle swarm optimization approach. Int. J. Hydrogen Energy 59, 51–62. https://doi.org/10.1016/j.ijhydene.2024.01.302.

Ali Abd, A., Naji, S.Z., Thian, T.C., et al., 2021. Evaluation of hydrogen concentration effect on the natural gas properties and flow performance. Int. J. Hydrogen Energy 46 (1), 974–983. https://doi.org/10.1016/j.ijhydene.2020.09.141.

Bian, J., Cao, X., Yang, W., et al., 2019. Condensation characteristics of natural gas in the supersonic liquefaction process. Energy 168, 99–110. https://doi.org/10.1016/j.energy.2018.11.102.

Blay-Roger, R., Bach, W., Bobadilla, L.F., et al., 2024. Natural hydrogen in the energy transition: fundamentals, promise, and enigmas. Renew. Sustain. Energy Rev. 189, 113888. https://doi.org/10.1016/j.rser.2023.113888.

Cao, X., Liu, Y., Zang, X., et al., 2021. Supersonic refrigeration performances of nozzles and phase transition characteristics of wet natural gas considering shock wave effects. Case Stud. Therm. Eng. 24, 100833. https://doi.org/10.1016/j.csite.2020.100833.

Cao, X., Yang, W., 2015. Numerical simulation of binary-gas condensation characteristics in supersonic nozzles. J. Nat. Gas Sci. Eng. 25, 197–206. https://doi.org/10.1016/j.jngse.2015.05.005.

Castier, M., 2014. Modeling and simulation of supersonic gas separations. J. Nat. Gas Sci. Eng. 18, 304–311. https://doi.org/10.1016/j.jngse.2014.03.014.

Cavana, M., Mazza, A., Chicco, G., et al., 2021. Electrical and gas networks coupling through hydrogen blending under increasing distributed photovoltaic generation. Appl. Energy 290, 116764. https://doi.org/10.1016/j.apenergy.2021.116764.

Chen, E., Fu, S., Yang, A., et al., 2023. Numerical sensitivity study on nucleation bulk tension factor of non-equilibrium condensation model. J. Mech. Sci. Technol. 37 (2), 977–985. https://doi.org/10.1007/s12206-023-0137-y.

Chen, J., Huang, Z., 2022. Spontaneous condensation of carbon dioxide in flue gas at supersonic state. Energy 254, 124418. https://doi.org/10.1016/j.energy.2022.124418.

Chen, J., Xu, Y., Huang, D., 2000. Geochemical characteristics and origin of natural gas in Tarim Basin, China. AAPG Bull. 84 (5), 591–606. https://doi.org/10.1306/c9ebce5f-1735-11d7-8645000102c1865d.

Choi, H., Lee, H., Han, J., et al., 2024. Revisiting the cost analysis of importing liquefied green hydrogen. Int. J. Hydrogen Energy 82, 817–827. https://doi.org/10.1016/j.ijhydene.2024.07.418.

Duan, H., Yin, X., Kou, H., et al., 2023. Regression prediction of hydrogen enriched compressed natural gas (HCNG) engine performance based on improved particle swarm optimization back propagation neural network method (IMPSO-BPNN). Fuel 331, 125872. https://doi.org/10.1016/j.fuel.2022.125872.

Economides, M.J., Wood, D.A., 2009. The state of natural gas. J. Nat. Gas Sci. Eng. 1 (1–2), 1–13. https://doi.org/10.1016/j.jngse.2009.03.005.

El-Emam, R.S., Özcan, H., 2019. Comprehensive review on the techno-economics of sustainable large-scale clean hydrogen production. J. Clean. Prod. 220, 593–609. https://doi.org/10.1016/j.jclepro.2019.01.309.

Faramawy, S., Zaki, T., Sakr, A.A., 2016. Natural gas origin, composition, and processing: A review. J. Nat. Gas Sci. Eng. 34, 34–54. https://doi.org/10.1016/j.jngse.2016.06.030.

Farhadian, A., Zhao, Y., Naeiji, P., et al., 2023. Simultaneous inhibition of natural gas hydrate formation and CO_2/H_2S corrosion for flow assurance inside the oil and gas pipelines. Energy 269, 126797. https://doi.org/10.1016/j.energy.2023.126797.

Ferreira, S.L.C., Bruns, R.E., Ferreira, H.S., et al., 2007. Box-Behnken design: An alternative for the optimization of analytical methods. Anal. Chim. Acta 597 (2), 179–186. https://doi.org/10.1016/j.aca.2007.07.011.

Gatto, A., Sadik-Zada, E.R., Lohoff, T., et al., 2024. An exemplary subsidization path for the green hydrogen economy uptake: Rollout policies in the United States and the European Union. J. Clean. Prod. 440, 140757. https://doi.org/10.1016/j.jclepro.2024.140757.

Girshick, S.L., Chiu, C.P., 1990. Kinetic nucleation theory: A new expression for the rate of homogeneous nucleation from an ideal supersaturated vapor. J. Chem. Phys. 93 (2), 1273–1277. https://doi.org/10.1063/1.459191.

Gyarmathy, G., 1982. The spherical droplet in gaseous carrier streams: Review and synthesis. Multiph. Sci. Technol. 1 (1–4), 99–279. https://doi.org/10.1615/multscientechn.v1.i1-4.20.

He, X., Kumakiri, I., Hillestad, M., 2020. Conceptual process design and simulation of membrane systems for integrated natural gas dehydration and sweetening. Sep. Purif. Technol. 247, 116993. https://doi.org/10.1016/j.seppur.2020.116993.

Júnior, C.J.C., Filho, P.D.A.P., 2023. Modeling and simulation of an industrial adsorption process of dehydration of natural gas in 4A molecular sieves: Effect of adsorbent aging. Results Eng. 18, 101144. https://doi.org/10.1016/j.rineng.2023.101144.

Jiang, T., He, X., Su, B., et al., 2024. COP 28: Challenge of coping with climate crisis. Innovation 5 (1), 100559. https://doi.org/10.1016/j.xinn.2023.100559.

Jiang, W., Bian, J., Liu, Y., et al., 2016. Investigation of flow characteristics and the condensation mechanism of ternary mixture in a supersonic nozzle. J. Nat. Gas Sci. Eng. 34, 1054–1061. https://doi.org/10.1016/j.jngse.2016.07.075.

Lakzian, E., Yazdani, S., Salmani, F., et al., 2024. Supersonic separation towards sustainable gas removal and carbon capture. Prog. Energy Combust. Sci. 103, 101158. https://doi.org/10.1016/j.pecs.2024.101158.

Liu, Y., Cao, X., Guo, D., et al., 2023. Influence of shock wave/boundary layer interaction on condensation flow and energy recovery in supersonic nozzle. Energy 263, 125662. https://doi.org/10.1016/j.energy.2022.125662.

Madadi Avargani, V., Zendehboudi, S., Cata Saady, N.M., et al., 2022. A comprehensive review on hydrogen production and utilization in North America: Prospects and challenges. Energy Convers. Manag. 269, 115927. https://doi.org/10.1016/j.enconman.2022.115927.

Neacsa, A., Eparu, C.N., Panaitescu, C., et al., 2023. Hydrogen–natural gas mix: A viable perspective for environment and society. Energies 16 (15), 5751. https://doi.org/10.3390/en16155751.

Netusil, M., Ditl, P., 2011. Comparison of three methods for natural gas dehydration. J. Nat. Gas Chem. 20 (5), 471–476. https://doi.org/10.1016/S1003-9953(10)60218-6.

Ogden, J., Jaffe, A.M., Scheitrum, D., et al., 2018. Natural gas as a bridge to hydrogen transportation fuel: Insights from the literature. Energy Policy 115, 317–329. https://doi.org/10.1016/j.enpol.2017.12.049.

Priya, R., Kanmani, S., 2011. Optimization of photocatalytic production of hydrogen from hydrogen sulfide in alkaline solution using response surface methodology. Desalination 276 (1–3), 222–227. https://doi.org/10.1016/j.desal.2011.03.053.

Ramírez-Ochoa, D.D., Pérez-Domínguez, L.A., Martínez-Gómez, E.A., et al., 2022. PSO, a swarm intelligence-based evolutionary algorithm as a decision-making strategy: A review. Symmetry 14 (3), 455. https://doi.org/10.3390/sym14030455.

Rouzbahani, A.N., Bahmani, M., Shariati, J., et al., 2014. Simulation, optimization, and sensitivity analysis of a natural gas dehydration unit. J. Nat. Gas Sci. Eng. 21, 159–169. https://doi.org/10.1016/j.jngse.2014.07.025.

Shan, S., Jin, G., Han, X., et al., 2025. Numerical study on the radiation characteristics of hydrogen-blended natural gas combustion. Combust. Sci. Technol. 1–27. https://doi.org/10.1080/00102202.2025.2536217.

Sun, S., Gu, L., Yang, Z., et al., 2022. Thermophysical properties of natural gas hydrates: A review. Nat. Gas Ind. B 9 (3), 246–263. https://doi.org/10.1016/j.ngib.2022.04.003.

Sun, W., Pen, J., Niu, L., et al., 2024. Sensitivity analysis of nucleation and droplet growth models in the prediction of natural gas non-equilibrium condensation in Laval nozzle. Appl. Therm. Eng. 236, 121562. https://doi.org/10.1016/j.applthermaleng.2023.121562.

Wang, S., Wang, C., Ding, H., et al., 2023. Joule-Thomson effect and flow behavior for energy-efficient dehydration of high-pressure natural gas in supersonic separator. Energy 279, 128122. https://doi.org/10.1016/j.energy.2023.128122.

Wen, C., Ding, H., Yang, Y., 2020. Optimisation study of a supersonic separator considering nonequilibrium condensation behaviour. Energy Convers. Manag. 222, 113210. https://doi.org/10.1016/j.enconman.2020.113210.

Yan, S., Jia, G., Du, J., et al., 2025. Water vapour condensation behaviour within hydrogen-blended natural gas in Laval nozzles. Case Stud. Therm. Eng. 69, 106064. https://doi.org/10.1016/j.csite.2025.106064.

Yang, Y., Shen, S., 2009. Numerical simulation on non-equilibrium spontaneous condensation in supersonic steam flow. Int. Commun. Heat Mass Tran. 36 (9), 902–907. https://doi.org/10.1016/j.icheatmasstransfer.2009.06.001.

Zhang, G., Zhang, S., Zhou, Z., et al., 2017. Numerical study of condensing flow based on the modified model. Appl. Therm. Eng. 127, 1206–1214. https://doi.org/10.1016/j.applthermaleng.2017.08.133.

Zhang, L., Jia, C., Bai, F., et al., 2024. A comprehensive review of the promising clean energy carrier: Hydrogen production, transportation, storage, and utilization (HPTSU) technologies. Fuel 355, 129455. https://doi.org/10.1016/j.fuel.2023.129455.

Zhang, Q., Chen, W., Ling, W., 2022. Policy optimization of hydrogen energy industry considering government policy preference in China. Sustain. Prod. Consum. 33, 890–902. https://doi.org/10.1016/j.spc.2022.08.017.

Zhao, Q., Liao, X., Ma, Z., et al., 2024. Comprehensive pollutant emission prediction models from hydrogen-enriched methane combustion in a gas-fired boiler based on Box-Behnken design method. Int. J. Hydrogen Energy 79, 728–740. https://doi.org/10.1016/j.ijhydene.2024.07.103.

Zhou, Z., Zhang, J., Huang, X., et al., 2019. Experimental study on distributed optical-fiber cable for high-pressure buried natural gas pipeline leakage monitoring. Opt. Fiber Technol. 53, 102028. https://doi.org/10.1016/j.yofte.2019.102028.

Zhou, Z., Zhang, J., Huang, X., et al., 2020. Trend of soil temperature during pipeline leakage of high-pressure natural gas: Experimental and numerical study. Measurement 153, 107440. https://doi.org/10.1016/j.measurement.2019.107440.